

**1 Spatial patterns of the tropical meridional circulation:
2 drivers and teleconnections**

3 Eli Galanti¹, Dana Raiter¹, Yohai Kaspi¹, and Eli Tziperman²

4 ¹Department of Earth and Planetary Sciences, Weizmann Institute of Science, Rehovot, Israel.

5 ²Department of Earth and Planetary Sciences and School of Engineering and Applied Sciences, Harvard
6 University, Cambridge, MA, USA

7 Key Points:

- 8** • Spatial patterns of the longitudinally-dependent meridional circulation (LMC),
found by clustering analysis, show zonal and meridional shifts.
- 9** • ENSO-driven SST is important in forcing the LMC variability, but the effect re-
quires more than the standard Nino3.4 and SOI indices.
- 10** • LMC patterns are also driven by the MJO, and affect other climatological vari-
ables such as remote surface air temperature and precipitation.
- 11**
- 12**
- 13**

14 **Abstract**

15 The large-scale Hadley circulation is a key element in the global heat and moisture trans-
 16 port. It is traditionally defined as the zonally-averaged meridional circulation in the trop-
 17 ics, but was shown to have a strong longitudinal dependence, as seen in a decomposi-
 18 tion of the three-dimensional atmospheric flow into spatially-dependent meridional and
 19 zonal circulations. Recent studies provided a useful analysis of the regional strengthen-
 20 ing/weakening of the decomposed circulation but not its patterns. Here we study the
 21 interannual variability of the longitudinally-dependent meridional circulation (LMC), with
 22 a focus on its spatial patterns. We use hierarchical clustering to objectively determine
 23 the four main modes of the LMC interannual variability, and apply a Lagrangian air par-
 24 cel tracking method to reveal the full circulation patterns. While El Niño and La Niña
 25 are found, as in previous studies, to play a role in setting these patterns, we find the pat-
 26 tterns are not uniquely characterized by standard ENSO indices (Nino3.4 or SOI). Instead,
 27 ENSO flavors (i.e., East Pacific vs. Central Pacific) have different effects on the LMC.
 28 The most prominent interannual variability of the LMC is an east-west shift. Latitudi-
 29 nal shifts, as well as contraction/expansion in both latitude and longitude are also iden-
 30 tified. Multiple linear regression analysis shows that while a large fraction of the LMC
 31 variance is explained by SST, the Madden-Julian Oscillation makes a non-negligible in-
 32 dependent contribution. The clustering patterns are also used to study the remote pre-
 33 cipitation and surface air temperature teleconnections.

34 **1 Introduction**

35 The Hadley circulation is a key element of the climate system (Hartmann, 1994),
 36 responsible for the energy and moisture transport from the equatorial region to the sub-
 37 tropics (e.g., Trenberth & Stepaniak, 2003). The circulation is commonly defined as the
 38 zonally-averaged meridional circulation in the tropical region (Hartmann, 2016), and is
 39 usually calculated as an annual mean or as an average over specific months or seasons.

40 The large longitudinal variations in the different elements involved in the Hadley
 41 circulation, such as the strength of the Inter Tropical Convergence Zone (ITCZ) and the
 42 location of the subtropical jets that mark the edges of the Hadley circulation, led to the
 43 need to calculate the contributions to the Hadley circulation at different longitudes. A
 44 method for calculating localized 2D circulations from the 3D wind field was first intro-
 45 duced by Keyser et al. (1989). Decomposing the wind field into a rotational and diver-
 46 gent components (Helmholtz decomposition), the longitudinally-dependent circulation
 47 can be derived from the divergent part of the flow. This method was implemented in sev-
 48 eral studies for the analysis of the meridional and zonal circulations in specific longitu-
 49 dinal sectors. It was first used to define the horizontal velocity potential and divergent
 50 wind in the upper troposphere, in which both the meridional circulation and the zonal
 51 circulation are manifested. This definition enabled the investigation of the global mon-
 52 son system and its relation to the two circulations on seasonal to decadal time scales
 53 (Trenberth et al., 2000; Tanaka et al., 2004). The Helmholtz decomposition was also ex-
 54 amined in comparison to a more general 3D decomposition of global atmospheric circu-
 55 lation (Hu et al., 2017).

56 Motivated by indications that the extent and strength of the Hadley circulation ex-
 57 hibit natural variability (e.g., Simpson, 2018), and might change in the coming century
 58 (e.g., Held & Soden, 2006; Grise et al., 2019; Chemke & Polvani, 2019), Helmholtz de-
 59 composition was also used to examine the natural variability and decadal change of the
 60 longitudinally dependent meridional circulation extent, either for specific sectors of the
 61 world (Nguyen et al., 2018), or directly as function of longitude (Staten et al., 2019). More
 62 recently, Raiter et al. (2020) used the same method, combined with a Lagrangian track-
 63 ing of air parcels, to examine in detail the mean tropical circulation, showing how the

64 longitudinally-dependent meridional circulation acts together with the subtropical jets
 65 to produce a tropical atmospheric conveyor belt.

66 Decomposition of the flow field into local meridional and zonal circulations was used
 67 to calculate the relative contributions of the vertical mass fluxes in the middle-troposphere
 68 to the meridional and zonal cells (Schwendike et al., 2014). Note that in that study, as
 69 well as in other studies, the local circulations are referred as Hadley and Walker circu-
 70 lations. Here we will use the more generic terms of meridional and zonal circulations,
 71 in order to avoid confusion with the classical definitions. The spatial distribution of ver-
 72 tical and meridional velocities were used also to calculate trajectories of climatological
 73 flow, emphasizing the regional aspects of the meridional circulation (Karnauskas & Um-
 74 menhofer, 2014). Examining the interannual variability of these two cells, Schwendike
 75 et al. (2014) found that the El Niño-Southern Oscillation (ENSO) has a much larger ef-
 76 fect on the local meridional circulation than on the local zonal circulation. This study
 77 was performed over specific longitudinal and latitudinal sectors, focusing on the Mar-
 78 itime continent. The same methodology was later used to study the inter-decadal trend
 79 of both the meridional and zonal circulations (Schwendike et al., 2015), where it was shown
 80 that in order to understand the effect of climate variability on the tropical circulation
 81 patterns, the analysis should be regional. The longitudinally-dependent circulations were
 82 also found to be correlated with different phases of the Madden-Julian Oscillation (Schwendike
 83 et al., 2021). The same method was also used to study specific regions of interest, such
 84 as the Atlantic sector of the meridional circulation during the Boreal summer and its con-
 85 nection to the Atlantic tropical cyclone activity (Zhang & Wang, 2013).

86 The examination of the interannual variability of the large scale circulation in the
 87 above studies was mostly limited to the strengthening/weakening of the meridional (or
 88 zonal) circulation at different sectors of the world, with less emphasis on the spatial changes.
 89 Another limitation of past studies is the methodology used for investigating the inter-
 90 annual variability, which was defined based on other modes of variability in the tropi-
 91 cal region, for example a state of El Niño or a state of La Niña. This makes the variabil-
 92 ity of the meridional circulation a mere reflection of the other modes of variability. There-
 93 fore, there is a need to define the modes of interannual variability of the local meridional
 94 circulation with a more objective method.

95 Here we study the interannual variability of the longitudinally-dependent merid-
 96 ional circulation (LMC) using clustering analysis, allowing an objective determination
 97 of the most important spatial patterns of variability. We then calculate the SST compos-
 98 ites for each LMC pattern (cluster). While previous studies (e.g., Schwendike et al., 2014)
 99 examined the interannual variability of the LMC by calculating its composites for El Niño
 100 and La Niña states, our approach allows examining the connection to climate variabil-
 101 ity modes without assuming such a connection to start with. We also use the cluster-
 102 ing patterns to characterize spatial shifts, widths and the spatial symmetry (skewness)
 103 of the LMC spatial patterns, and their dependence on the SST. In addition, we use a La-
 104 grangian perspective to tie these modes to the actual 3D changes in the air flow. We use
 105 multiple linear regression analysis to link the LMC variability to the SST and the Madden-
 106 Julian Oscillation (MJO), as well as to remote precipitation and surface air temperature
 107 patterns.

108 The manuscript is organized as follows: in section 2 we present the method by which
 109 the local meridional circulation is calculated and the method for clustering its interan-
 110 nual variability. The results are shown in section 3, with the characteristics of the LMC
 111 spatial patterns discussed in section 3.1, and the relation to other climatic variables dis-
 112 cussed in section 3.2. We conclude in section 4.

113 **2 Data and methods**114 **2.1 The longitudinally-dependent meridional circulation**

115 We use three data sets to ensure robustness of our analysis: the European Center
 116 for Medium range Weather Forecasts ERA-Interim reanalysis (Dee et al., 2013), their
 117 newer ERA5 reanalysis (Hersbach et al., 2020), and the National Centers for Environ-
 118 mental Prediction (NCEP) reanalysis II (Kanamitsu et al., 2002). In our analysis we use
 119 the monthly mean data covering the years 1979–2018. All three data sets are used to per-
 120 form the analysis, but in the results we show the Era-Interim data. This data set was
 121 extensively used in recent studies discussing the large scale tropical circulation, especially
 122 in relation to the longitudinal variability, which is our focus here(e.g., Schwendike et al.,
 123 2014, 2015; Schwendike et al., 2021; Grise et al., 2019; Guo & Tan, 2018; Hu et al., 2017;
 124 Karnauskas & Ummenhofer, 2014; Nguyen et al., 2018). In order to make a meaning-
 125 ful and direct comparison to these works, we choose to use the same data set in the main
 126 text, but also show the results for the NCEP2 and ERA5 in the Supporting Information
 127 (SI).

128 The mass-weighted global meridional circulation (Hartmann, 2016) is represented
 129 by a stream function calculated using the zonally-averaged meridional velocity \bar{v}

$$\psi(\phi, p, t) = \frac{2\pi a \cos \phi}{g} \int_0^p \bar{v}(\phi, p', t) dp', \quad (1)$$

130 where a is Earth's radius, g is the gravitational acceleration, ϕ is latitude, and p is pres-
 131 sure. The time average of this circulation is shown in Fig. 1a. The two classical Hadley
 132 cells can be seen roughly between the equator and latitudes $\pm 30^\circ$. However, the circu-
 133 lation, as defined by Eq. 1, cannot account for any zonal asymmetry in the meridional
 134 circulation. The longitudinally-dependent meridional circulation can be calculated via
 135 the separation of the 3D wind velocity field into a meridional component and a zonal one.
 136 Here we follow the notation of Hu et al. (2017). First, the divergence of the wind is cal-
 137 culated

$$D = \nabla \cdot \vec{V}, \quad (2)$$

138 where $\vec{V} = (u, v)$ is the full horizontal wind vector. Then, the velocity potential χ is
 139 calculated via

$$\nabla^2 \chi = D. \quad (3)$$

140 This equation can be solved either via decomposition into spherical harmonics, or by for-
 141 mulating the problem as a set of finite difference linear equations and inverting the Lapla-
 142 cian. The methods are equivalent and in this study the latter is used. The potential func-
 143 tion is then used to calculate the divergent wind

$$\nabla \chi = \vec{V}_{\text{div}}, \quad (4)$$

144 where $\vec{V}_{\text{div}} = (u_{\text{div}}, v_{\text{div}})$. The zonal (meridional) component of the divergent wind is
 145 associated with closed east-west (north-south) oriented circulations, such as the Walker
 146 (Hadley) cell. Therefore, the divergent wind can be used, similar to Eq. 1, to calculate
 147 the longitudinally-dependent meridional circulation

$$\psi(\lambda, \phi, p, t) = \frac{1}{g} \int_0^p v_{\text{div}}(\lambda, \phi, p', t) dp', \quad (5)$$

148 where λ is longitude. Note that the integral of Eq. 5 over longitude gives the classical
 149 zonally averaged meridional circulation (Eq. 1). A simplified representation of the merid-
 150 ional circulation can be defined by averaging ψ between 600 – 400 hPa

$$\tilde{\psi}(\lambda, \phi, t) = \frac{1}{\Delta p} \int_{p_1}^{p_2} \psi(\lambda, \phi, p', t) dp', \quad (6)$$

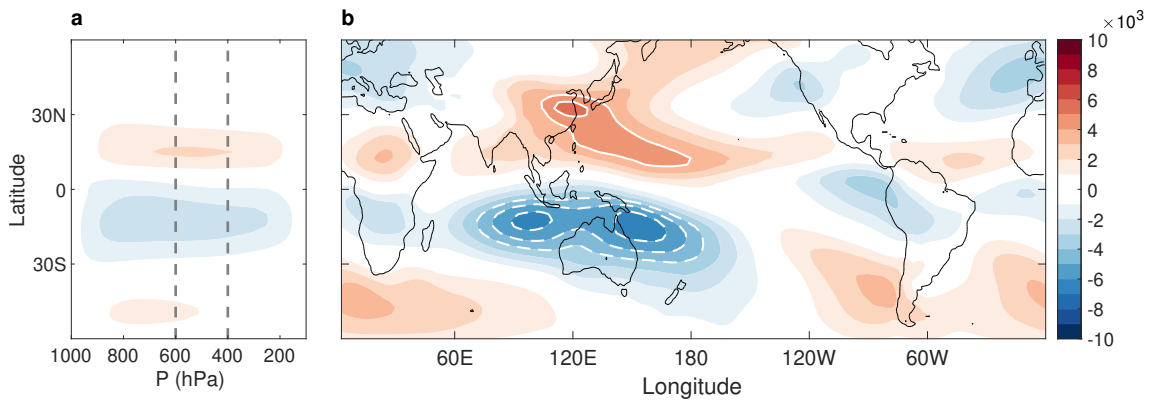


Figure 1. The climatological meridional circulation. (a) The zonally averaged circulation (Hadley cells) as function of latitude and pressure with the dashed lines denoting the 400 and 600 hPa. (b) The annual average of the meridional longitudinally-dependent circulation, averaged between 400 and 600 hPa, as function of longitude and latitude. Contour interval is $1 \times 10^3 \text{ kg s}^{-1} \text{ m}^{-1}$. White solid and dashed lines indicate absolute values larger than $4 \times 10^3 \text{ kg s}^{-1} \text{ m}^{-1}$.

151 where $p_1 = 400 \text{ hPa}$, $p_2 = 600 \text{ hPa}$, and $\Delta p = p_2 - p_1$. As discussed above this is the
 152 region where the zonal mean meridional circulation reaches its maximum. We will use
 153 this simplified definition of the local meridional circulation (denoted hereafter as LMC)
 154 throughout this study. The time averaged LMC is shown in Fig. 1b. It has a very strong
 155 zonal dependence — it is most pronounced in the Indo-Pacific region, between 70° – 180° E,
 156 and is much stronger in the Southern hemisphere.

157 2.2 Interannual variability analysis using hierarchical clustering

158 The temporal variability of the LMC can be explored using cluster analysis, in which
 159 spatial patterns that are prone to repeat in time are identified. Unlike methods based
 160 on principal components requiring that the different patterns are orthogonal to each other,
 161 clustering allows the identification of commonly occurring patterns that may not be or-
 162 thogonal. There are several methods to perform cluster analysis; here we use hierarchi-
 163 cal clustering that was successfully applied to the studies of atmospheric dynamics (e.g.,
 164 Cheng & Wallace, 1993; Kao & Yu, 2009; Horton et al., 2015; Totz et al., 2017). Other
 165 variants of the clustering method such as the *k-means* (e.g., Madonna et al., 2017) and
 166 self organizing maps (e.g. Feldstein & Lee, 2014) were used in climate studies. The data
 167 used here — the monthly-mean longitudinally-dependent meridional circulation at each
 168 time step averaged over 400–600 hPa, is treated as an N dimensional vector where N
 169 is the number of grid points. Note that to isolate the interannual variability we remove
 170 the seasonal cycle from the data (via the subtraction of the twelve monthly averages from
 171 the corresponding points of the monthly data). We analyze two data sets simultaneously,
 172 so that the number of samples is twice over the time span, thus increasing the robust-
 173 ness of the identified clusters. The method allows to find how the 960 vectors (2 data
 174 sets \times 40 years \times 12 months) are clustered in the N -dimensional space. Note that the
 175 analysis was repeated with different combinations of the data sets. Starting with the as-
 176 sumption that each point of the entire data set is a single cluster, the method then per-
 177 forms a hierarchical separation of the data to a decreasing number of clusters, combin-
 178 ing previously identified clusters into new clusters using the Ward method of combin-
 179 ing clusters based on minimal increase in cluster variance (Wilks, 2011). One then needs
 180 to decide what the optimal number of clusters is.

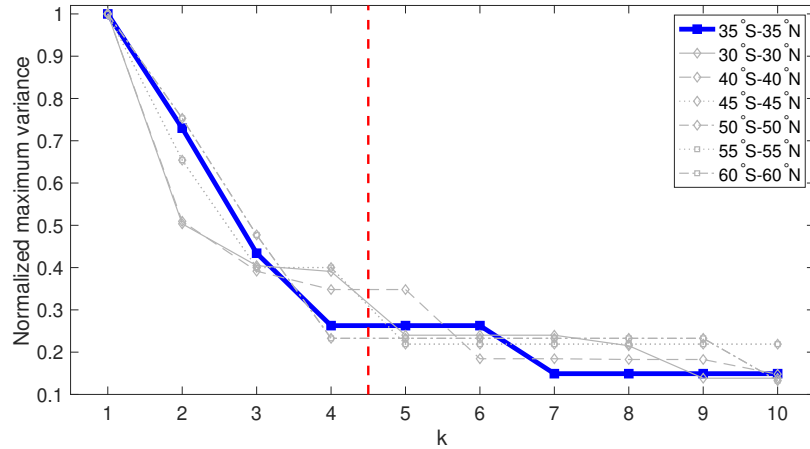


Figure 2. Normalized maximal cluster variance as function of the number of clusters used in the analysis. Shown is the analysis with data restricted to the latitudinal range of 35°S-35°N (blue), and the analysis for other latitudinal ranges. Dashed red line denotes the 4 clusters cutoff used in the analysis.

For the clustering analysis, we examine the meridional circulation in latitudinal range 35°S-35°N, where the LMC is most significant (Fig. 1). Plotting the maximal cluster variance as function of the number of clusters, the optimal number of clusters can be identified (Fig. 2, blue line). By definition, increasing the number of clusters results in a smaller variance (data vectors are better clumped together). However, the maximum cluster variance decreases substantially in the range of up to 4 clusters, while further increasing the number of clusters does not result in a significant reduction. Repeating the analysis for different latitudinal ranges results in a similar conclusion, strengthening the robustness of the analysis. Note that Kao and Yu (2009), who analyzed the interannual variability of the Pacific SST using hierarchical clustering, also found that 4 clusters best describe the variability of the SST. Finally, even though a given month from the two chosen data sets (ERA-Interim and NCEP, or ERA-Interim and ERA5) may be assigned to two different clusters, in practice each of the 4 clusters are found to contain predominantly the same months in each of the two data sets (only 8 of the 480 months are different for the first choice, none were different for the latter). Moreover, all the results discussed in this study are evident in all data sets, i.e., the composites calculated for each cluster are similar, showing that the interannual variability of the LMC, as depicted by the clustering analysis, is robust over different data sets (see SI, Figures S1 to S3). In order to allow a direct comparison with previous studies (see above discussion), the results shown here are based on the ERA-Interim data, while the results for the two data sets are shown in the SI.

3 Results

We start by examining the occurrence of monthly data points that are assigned to each cluster, as function of time from 1979 to 2018, and as function of time during the year. Fig. 3a shows the occurrence of the 4 clusters C_1, C_2, C_3, C_4 in different colors, marked over a time series of the Nino3.4 Index (SST anomalies averaged over 5°N-5°S, 120°-170°W, with a 5-month running average). The Nino3.4 represents ENSO phenomenon, the leading mode of interannual variability in the tropics (e.g., Wang et al., 2017). ENSO events are typically defined when the Nino3.4 value exceeds $\pm 0.4^{\circ}\text{C}$ (gray dashed lines) for at least 6 consecutive months. We begin with a more qualitative examination of the relation between the clusters and El Niño/La Niña, and below analyze this more quantita-

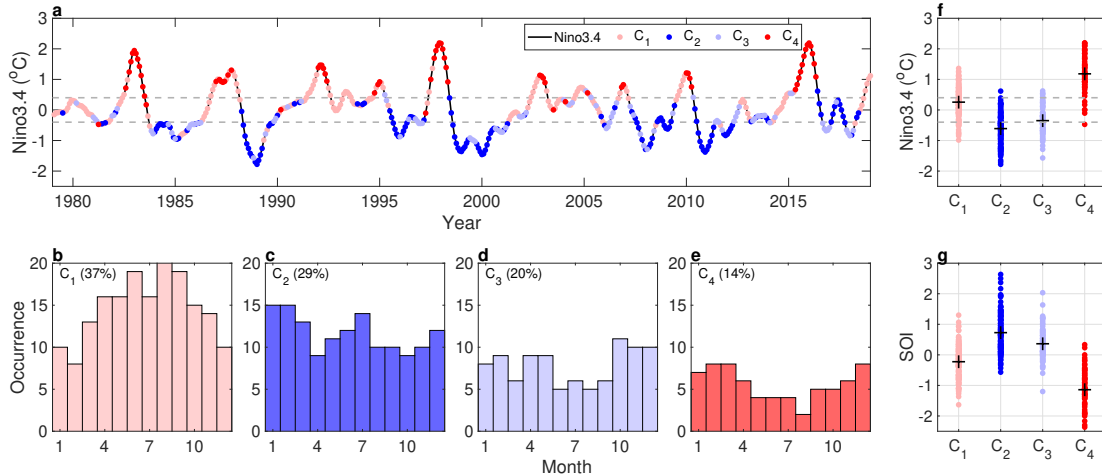


Figure 3. The time occurrence of the LMC interannual variability clusters. (a) The occurrence of each cluster plotted as colored dots on top of the ENSO Nino3.4 index. (b-e) The occurrence of each cluster as function of the month of the year. Also shown is the total occurrence percentage of each cluster. (f) The occurrence of each cluster as function of the Nino3.4 index. (g) The occurrence of each cluster as function of the SOI index. Horizontal dashed lines in (a) and (f) denote the $\pm 0.4^{\circ}\text{C}$ threshold used to define ENSO events.

tively. Points in the first cluster (marked by light red dots) seem to occur mostly during periods when the Nino3.4, is weakly positive, and correspond to 37% of the analyzed months. The second cluster (blue) corresponds mostly to periods when the Nino3.4 is strongly negative (29% of months), and the third cluster (light blue) represents mostly periods when the Nino3.4 is weakly negative (20%). The fourth cluster (red) mostly represents periods when the Nino3.4 is strong positive (14%). Also shown is the month of the year of data vectors assigned to each cluster (Fig. 3b-e). Months assigned to cluster C_1 occur more frequently during the northern hemisphere summer, while those in C_4 appear more during the northern hemisphere winter. On the other hand, months assigned to clusters C_2 and C_3 have only a weak dependence on the month of the year.

Previous work assumed the variability of the LMC to be dominated by ENSO and calculated it for different phases of the ENSO cycle based on the Nino3.4 Index (e.g., Nguyen et al., 2018), or the Southern Oscillation Index (SOI, e.g., Schwendike et al. (2014)). Our methodology allows us to examine this hypothesis, as we calculate the LMC patterns using cluster analysis independently of the state of ENSO. Fig. 3f-g shows the Nino3.4 and SOI indices, respectively, for all months of each LMC cluster. While our above discussion and Fig. 3a suggest some relation between different clusters and the ENSO phases, the analysis in Fig. 3f-g shows very clearly that there is no direct one-to-one correspondence between the two. Instead, there is a significant overlap in the Nino3.4 and SOI values for months corresponding to the different LMC patterns. Moreover, during some El Niño events cluster C_1 is present for a considerable part of the event duration, and in some events even more than C_4 , for example, during the 1986-1987, 1991-1992, 2002-2003, and 2009-2010 events. However, the same cluster is also frequently present during periods with Nino3.4 weakly positive, and even during periods when Nino3.4 is negative. Similar arguments can be made for C_2 and C_3 , both of which are present during periods when Nino3.4 is only weakly negative and during periods when it is strongly negative (La Niña events). We conclude that LMC patterns are not uniquely determined by the state of ENSO as quantified by these standard indices, a result that may not be very surprising given the diversity of ENSO spatial patterns and the inability of any scalar

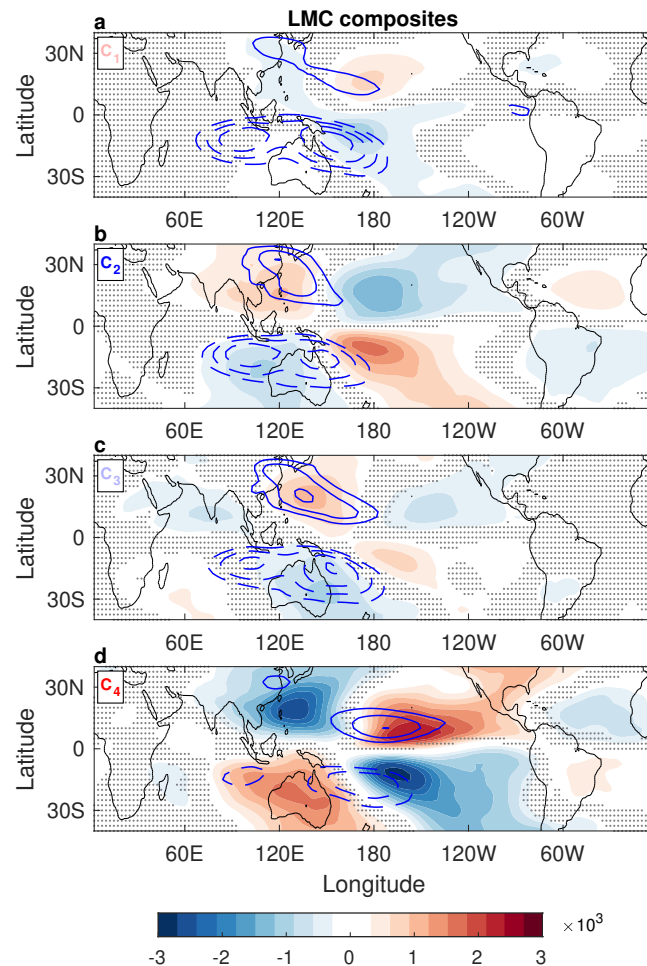


Figure 4. Composites of the anomalous LMC for each of the 4 clusters (shadings, in $\text{kg s}^{-1} \text{m}^{-1}$), and the full LMC composites for the months of each cluster (blue lines, with same values as a in Fig. 1b). Dotted areas indicate regions where the cluster is not statistically significant.

index to represent it. We will see below (section 3.2) that there is still a relation between the LMC clusters and different flavors of ENSO as was hypothesized in previous work, even if it cannot be expressed in terms of these indices as was assumed previously.

3.1 Quantifying the spatial characteristics of different LMC patterns

Based on the classification of each of the 480 months in the data set, a composite of the LMC is calculated for each cluster from the ERA-Interim data set (Fig. 4). Note that composites based on the NCEP and ERA5 reanalyses give very similar spatial patterns, showing that the clusters are robust over different data sets (SI, Fig. S1). For each composite we calculate the 95% confidence level using a non-parametric two-sided statistical test, where the absolute value of the cluster at each grid point is verified to be larger than the one calculated with a random selection of months, 95% of the times. Marking the regions where the results are not statistically significant with gray dots, it is clear that the cluster structure is significant in all regions where the clusters have large values.

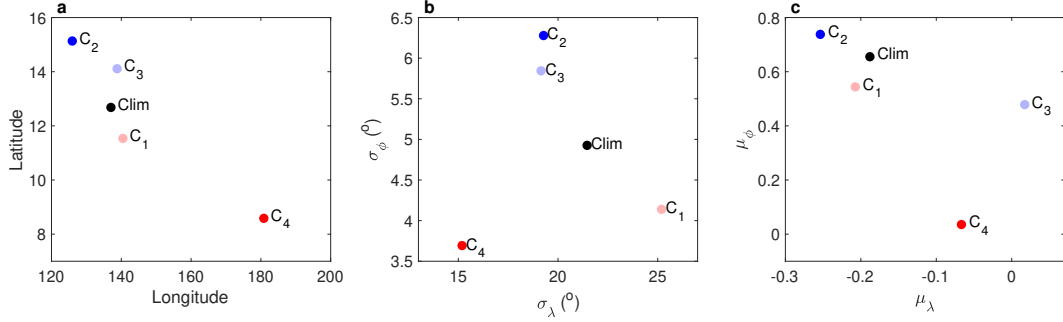


Figure 5. The spatial characteristics for each cluster and the DJF climatology. Shown are: (a) center of mass, (b) the standard deviation, and (c) the skewness. The colors denoting each cluster are the same used in Fig. 3.

The anomalies represented by the clusters are all antisymmetric about the equator, an indication of a similar weakening or strengthening of the circulation in both the northern and southern hemisphere LMC. Below we discuss this aspect in relation to the SST analysis (Section 3.2.1). The clusters also show an east-west asymmetry, peaking around a longitude range between 90°E and 150°W. The pattern of two maxima and two minima indicates a shift of the LMC either eastward (C_1 and C_4) or westward (C_2 and C_3) relative to climatology. This zonal movement of the meridional circulation was indirectly observed in relation to ENSO (Feng et al., 2017; Guo & Tan, 2018), and could be viewed as part of the shifts in the Walker circulation during ENSO events (e.g., Tanaka et al., 2004), however its direct identification is made possible in our study due to the definition of the LMC. In addition, the patterns indicate that the LMC also shows variability in its latitudinal location, width and north-south skewness. In order to quantify these variations, we define the LMC most significant region as the region with values larger than $7 \times 10^3 \text{ kg s}^{-1} \text{ m}^{-1}$, and calculate the weighted average location, standard deviation, and skewness for each cluster

$$\begin{aligned} (\bar{\lambda}_i, \bar{\phi}_i) &= \frac{\sum(\lambda, \phi)\tilde{\psi}_i}{\sum\tilde{\psi}_i}, \quad (\sigma_{\lambda,i}, \sigma_{\phi,i}) = \frac{\sum([\lambda - \bar{\lambda}_i]^2, [\phi - \bar{\phi}_i]^2)\tilde{\psi}_i}{\sum\tilde{\psi}_i}, \\ (\mu_{\lambda,i}, \mu_{\phi,i}) &= \frac{\sum([\lambda - \bar{\lambda}_i]^3, [\phi - \bar{\phi}_i]^3)\tilde{\psi}_i}{(\sigma_{\lambda,i}^3, \sigma_{\phi,i}^3)\sum\tilde{\psi}_i}, \end{aligned} \quad (7)$$

where $(\bar{\lambda}_i, \bar{\phi}_i)$, $(\sigma_{\lambda,i}, \sigma_{\phi,i})$, and $(\mu_{\lambda,i}, \mu_{\phi,i})$, are the longitude and latitude of the center, the standard deviation, and the skewness of the LMC cluster, respectively, and $\tilde{\psi}_i$ is the LMC averaged over the DJF months of the i th cluster.

The shifts and skewness of the LMC are summarized in Fig. 5. Most apparent is the eastward shift of the center locations during strong El Niño (C_4) (Fig. 5a), with a longitudinal shift of around 50 degrees. During the strong La Niña related months (cluster C_2), the LMC is shifted by about 15 degrees to the west. In addition, there is an up to 4 degrees north-south shift of the LMC center, where C_1 and C_4 are shifted to the south, and C_2 and C_3 to the north. The longitudinal extent of the LMC (Fig. 5b) does not change much for the different clusters, but the latitudinal extent does exhibit a clear shift, where C_1 and C_4 are getting narrower, and C_2 and C_3 wider. Together with the shift of the mean location, this implies that the LMC is more equatorially confined during C_1 and C_4 than during C_2 and C_3 . This finding is consistent with the behavior of the zonally-averaged Hadley circulation during ENSO (Oort & Yienger, 1996; Caballero, 2007), but with our longitudinally-depended analysis it is even more pronounced. Fig. 5a

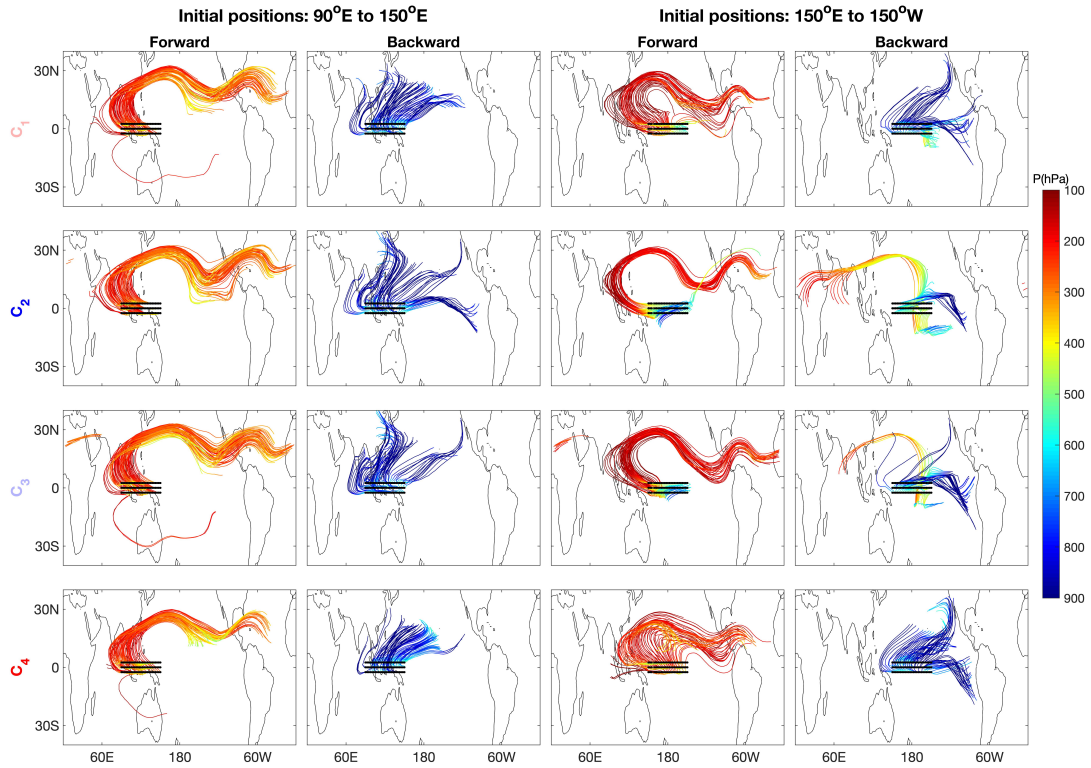


Figure 6. Trajectories of air parcels during DJF months associated with each cluster. Initial positions are set around the equator in two main regions: 90°E to 150°E , and 150°E to 150°W . The air parcels are initiated from a height of 500 hPa and followed for 20 days forward, and 20 days backward. The color indicates the height (hPa) of the parcel during its trajectory.

285 shows negative correlation between the shifts in the zonal and meridional directions, while
 286 panel b shows that there is no obvious relation between the extent of the clusters in lat-
 287 itude and longitude. Looking at the change in the skewness (Fig. 5c) we see that dur-
 288 ing C_4 the north-south asymmetry disappears. These morphological changes in the LMC
 289 indicate that the interannual variability of the large scale tropical circulation is not lim-
 290 ited to strengthening and weakening, but also involves significant shifts. Next, we ex-
 291 plore how these modifications are expressed in the full 3D flow.

292 Since the LMC, as calculated and plotted above, captures only the meridional com-
 293 ponent of the tropical large-scale circulation, a better understanding of the changes on
 294 interannual time scales in the actual 3D circulation can be achieved using a Lagrangian
 295 perspective, in which air parcels trajectories are followed given an initial position (Raiter
 296 et al., 2020). Note that a similar methodology was used by Feng et al. (2017) to study
 297 ENSO teleconnections. The full circulation, depicted by the Lagrangian analysis, is af-
 298 fected not only by the LMC but also by the zonal circulation and by the rotational (hor-
 299 izontal) circulation (e.g., Raiter et al., 2020). Based on the cluster analysis (Fig. 4), we
 300 set two regions of initial positions around the equator, one between 90°E and 150°E , and
 301 another between 150°E and 150°W (Fig. 6, black dots). These regions cover the main
 302 dipole signal in the 4 clusters. The air parcels initial positions are set at a height of 500 hPa,
 303 and are followed for 20 days forward and 20 days backward in time. This allows a suf-
 304 ficient coverage of the full tropical circulation (see Raiter et al. (2020) for a detailed dis-

305 cussion of the methodology). We examine the circulation during the averaged flow con-
 306 ditions in the months associated with each cluster. Since the tropical circulation has a
 307 significant seasonal cycle, we define the states using only the DJF months, but a sim-
 308 ilar behavior (in the opposite hemisphere) is apparent when looking at the JJA months.
 309 Note also that the characteristics of the trajectories in all 4 clusters and for the two re-
 310 gions or initial position were found to be similar in all three data sets. In the SI (Fig. S2
 311 and S3) we show the analysis for all data sets.

312 We start with a general description of the longitudinally-dependent meridional cir-
 313 culation that is common to all clusters during DJF. The air, rising over the maritime con-
 314 tinent, moves westward with the trade winds, then northward with the LMC, and then
 315 enters the jet streams moving eastward. Part of the circulation descends in the mid-Pacific
 316 and part descends over the Americas (Raier et al., 2020). The backward trajectories show
 317 how the air is converging to the equatorial region from the lower altitude central and east-
 318 ern Pacific, mostly from the northern hemisphere.

319 The interannual variability is apparent in the different trajectories driven by the
 320 circulation associated with each of the clusters. First, we look at the most distinct clus-
 321 ters, C_2 (La Niña related) and C_4 (El Niño related). During months corresponding to
 322 C_4 , the western region (left panels) exhibits a weaker and more confined circulation, than
 323 during C_2 ; this is expected, given that the circulation moves eastward during El Niño
 324 events. Conversely, in the eastern region (right panels), a much more pronounced merid-
 325 ional circulation is observed during C_4 . During C_2 months, the air parcels either stay
 326 in place or move to the Western Pacific before going north, consistent with the circu-
 327 lation moving west during La Niña events, while during C_4 conditions, air parcels move
 328 directly upward and to the north. In addition, during C_2 conditions, the air parcels origi-
 329 nating in the western region are affected by a much stronger and larger-scale circula-
 330 tion than in the climatology. The east-west shift between C_2 and C_4 is also apparent in
 331 the back trajectories on the second and fourth columns of Fig. 6. These features of the
 332 full 3D trajectories are consistent with the analysis of the LMC in Fig. 5, also showing
 333 significant shifts in the east-west and north-south directions, as well as changes in the
 334 latitudinal extent of the circulation.

335 Further details on the complexity of the relation between the LMC variability and
 336 ENSO are revealed by clusters C_1 and C_3 . For example, during C_3 , air parcels originat-
 337 ing from the eastern initial positions (Fig. 6, third column) move farther to the east than
 338 all other clusters. After 20 days, these parcels reach the Middle East, while in the other
 339 clusters they only reach Western Europe. Thus C_3 is not merely a weak version of C_2 ,
 340 although both are associated with periods when Nino3.4 is negative. Similarly, some of
 341 the parcels originating from the western region (Fig. 6, first column) during C_1 reach fur-
 342 ther to the west than during C_3 , even though the former is associated with periods when
 343 the Nino3.4 is positive and the latter when it is negative.

344 3.2 Drivers and teleconnections of LMC variability

345 3.2.1 Drivers of the LMC variability

346 The classification of the temporal variations of the LMC into the 4 clusters can be
 347 used to search for accompanying variability in other oceanic and atmospheric variables
 348 that might act as drivers for the LMC. We now calculate SST composites for each LMC
 349 cluster (seasonal cycle removed similarly to the LMC, Fig. 7a-d). The ENSO signal is
 350 clearly identified in the strong SST anomalies at the central to east equatorial Pacific,
 351 with C_2 and C_3 associated with a La Niña phases and C_1 and C_4 with an El Niño phases.
 352 The 4 SST patterns are overall symmetric around the equator, mostly in the Central Pa-
 353 cific region, which is a characteristic of ENSO. If the LMC-SST relation is indeed strong
 354 (as we will demonstrate below), this explains why the LMC patterns (Fig. 4) also ex-
 355 hibit symmetry around the equator.

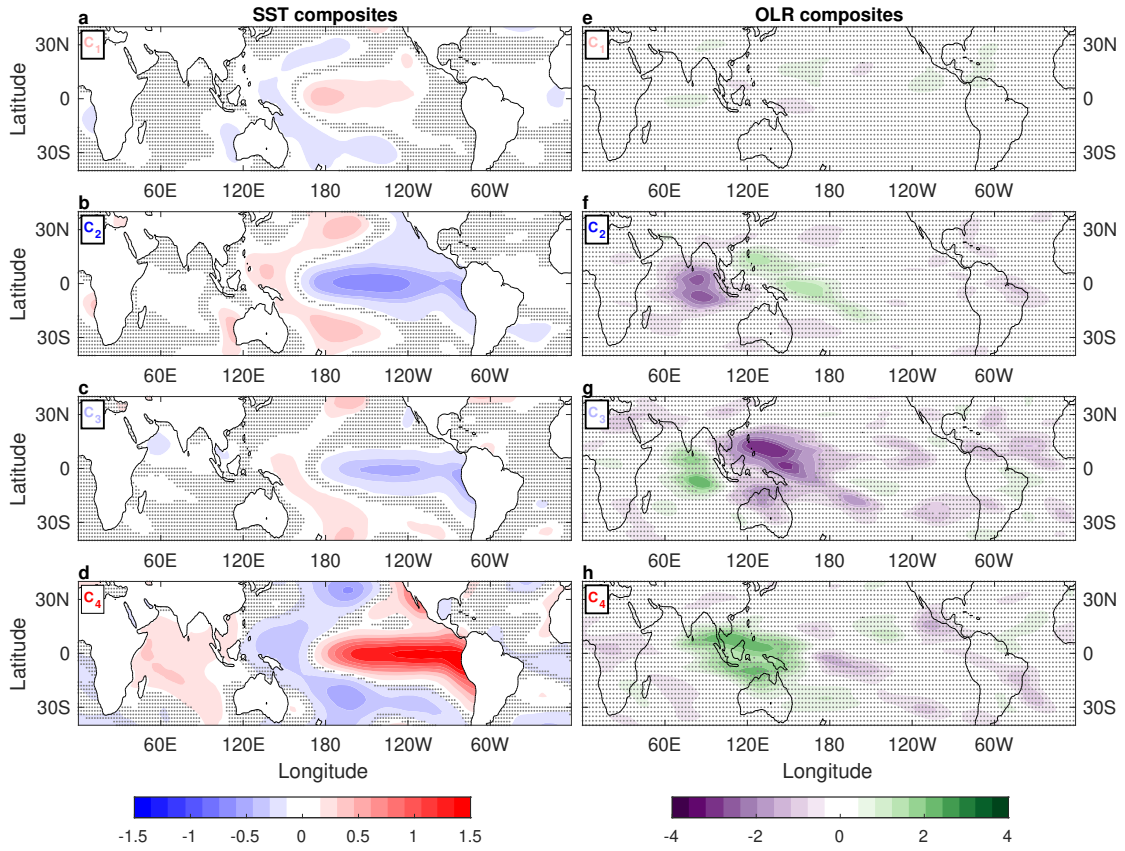


Figure 7. (a-d) Composites of SST anomalies for each of the clusters (in $^{\circ}\text{C}$). (e-h) Composites of 10–90 days bandpass OLR (W m^{-2}). Regions below the 95% confidence level are marked with gray dots.

The two pairs of clusters reveal the action on the LMC by the different ENSO flavors (Kao & Yu, 2009; Capotondi et al., 2015). In the positive SST-related clusters, C_4 relates to a more classical eastern Pacific (EP) El Niño (e.g., Rasmusson & Carpenter, 1982), while C_1 relates to a central Pacific (CP) El Niño, also referred to as El Niño Modoki (Ashok et al., 2007). In the negative SST-related clusters, C_2 relates more to CP La Niña, and C_3 relates more to EP La Niña. These relations are also apparent in the temporal variations of the LMC clusters (Fig. 3a), similar to those found for the SST variability (Fig. 1, Capotondi et al., 2015): The 2004–2005 (1997–1998) El Niño event is characterized mostly by C_1 (C_4) LMC clusters, and the 1988–1989 (2007–2008) La Niña event is characterized mostly by C_2 (C_3). Furthermore, the SST patterns associated with the LMC (Fig. 7a-d) bear some resemblance to the 4 SST patterns found by Kao and Yu (2009) to best describe the Eastern and Central Pacific ENSO events, strengthening the role of the spatially-dependent SST interannual variability in setting the LMC.

We would like next to determine to what degree can a given driver, such as the SST, be related to the LMC variability using regression analysis between the time series representing the variability in the driver and in the LMC. For this purpose, the LMC is projected on each of its cluster averages $C_i(\lambda, \phi)$ shown in Fig. 4,

$$\tilde{\psi}_i(t) = \frac{1}{2\pi\Delta\phi} \int_{\phi=-\frac{\pi}{3}}^{\frac{\pi}{3}} \int_{\lambda=0}^{2\pi} \tilde{\psi}(\lambda, \phi, t) C_i(\lambda, \phi) \cos \phi d\lambda d\phi, \quad (8)$$

Table 1. The dependence of the LMC on the SST and MJO (Eq. A1), and the dependence of air temperature and precipitation on the LMC and SST (Eqs. 10,11), for the 4 clusters. Shown are the multi-linear regression coefficients, and the R^2 for each case.

	LMC			Air Temperature			Precipitation		
	SST (β_L)	MJO (γ_L)	R^2	LMC (β_T)	SST (γ_T)	R^2	LMC (β_P)	SST (γ_P)	R^2
C_1	0.80	0.09	0.64	0.21	0.39	0.33	0.81	0.09	0.78
C_2	0.82	0.24	0.74	0.15	0.77	0.82	0.89	0.06	0.88
C_3	0.76	0.27	0.65	0.16	0.73	0.75	0.87	0.06	0.85
C_4	0.84	0.25	0.77	0.04	0.84	0.77	0.73	0.25	0.90

and the resulting time series are then normalized by their standard deviation. Similarly, all other fields are projected onto their respective cluster-average composites and normalized.

The dependence of the LMC on the SST is now revealed by calculating the regression,

$$LMC(t) = \alpha_L + \beta_L SST(t). \quad (9)$$

The fraction of variance explained by the SST for C_2 , C_3 , and C_4 is around 68%, 58%, and 71%, respectively.

While the above analysis (as well as previous studies, e.g., Schwendike et al., 2014) indicates that LMC variability is closely related to SST anomalies, it might also be influenced by other atmospheric phenomena (Schwendike et al., 2021). Given that the Madden-Julian Oscillation (MJO, Madden & Julian, 1971; Zhang, 2005) is the largest intraseasonal signal in the tropics, we attempt to find connections to this signal as well, with detailed analysis in Appendix A, briefly summarized here. The MJO-related OLR composites for each cluster are shown in Fig. 7e–h. The structure of the composites resembles different phases of the MJO (Wheeler & Hendon, 2004): C_2 is similar to MJO phase 6, C_3 is similar to phases 2 and 3, and C_4 is similar to phase 5. Note that the composites of the two La Niña related clusters (C_2 and C_3 , Fig. 7b,c) correspond to opposite phases of the MJO (Fig. 7f,g), supporting the MJO being a separate driver from the ENSO-related SST. A multivariate regression analysis of the LMC as function of both the normalized SST and normalized MJO (Table 1 and Appendix A) shows that the MJO explains some 6–7% of the LMC variance for clusters $C_{2,3,4}$, indicating that the MJO effects are weak yet non-negligible, consistent with the findings of, e.g., Seo et al. (2016); Schwendike et al. (2021).

3.2.2 Teleconnections involving LMC variability

Next, we relate the variability of the LMC to the variability of air temperature at 2 meters and of the total precipitation, both fields of obvious socioeconomic relevance. The two fields are expected to be influenced by the magnitude and patterns of the LMC, or at least be closely related to these patterns. A stronger LMC implies more upward motion in the tropics and therefore stronger precipitation. At the same time, of course, latent heat release due to this precipitation may drive atmospheric motions related to the LMC. Similarly, surface air temperature over the equatorial Pacific is expected to be closely coupled with the SST and therefore be a driver, yet remote signals are more likely to be consequences of the LMC variability and of the ENSO variability that drives it. It is therefore difficult to clearly identify consequences vs drivers here, but the rela-

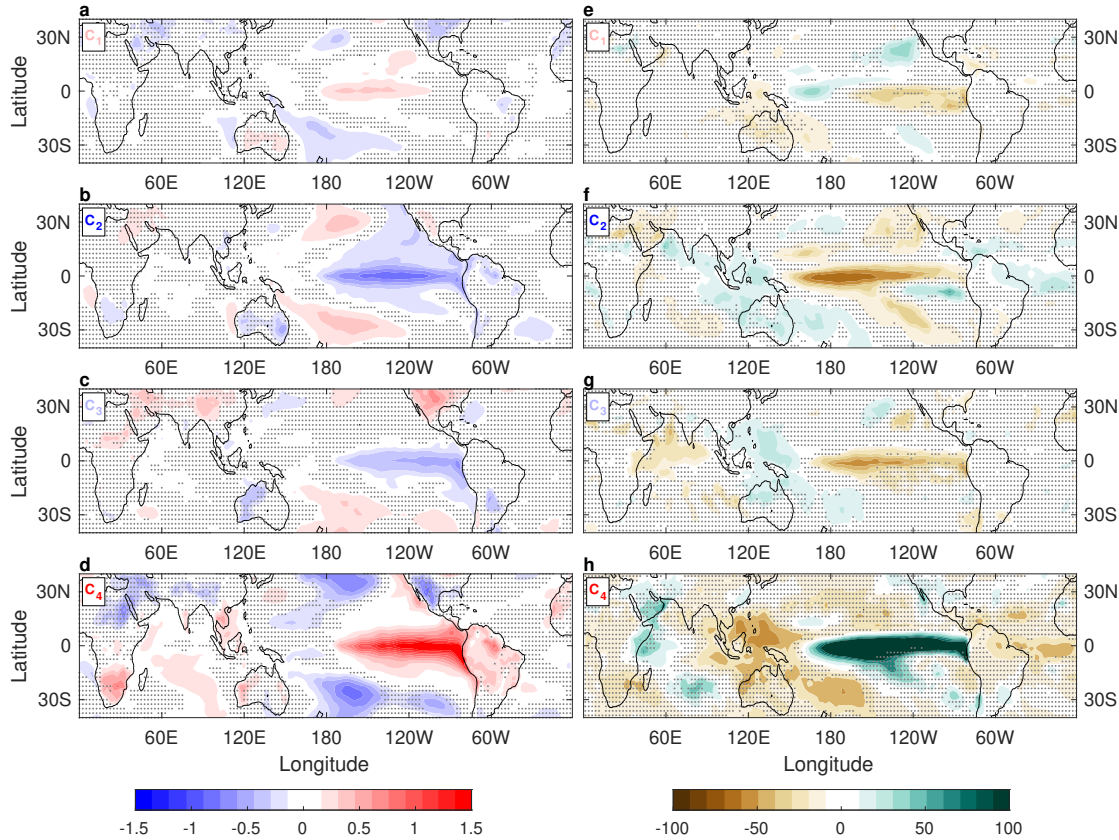


Figure 8. Same as in Fig. 4 but (a-d) for the 2 meter air temperature (in °C), and (e-h) for the fractional precipitation change (in percentage).

tion to these fields is clearly interesting and important and this issue is further discussed below.

The composites for the surface air temperature and precipitation are shown in Fig. 8, and are statistically significant where the amplitude is substantial, indicating that the interannual variability of both air temperature and precipitation is strongly correlated with the LMC variability. There are major differences between the fields: the precipitation variability (Fig. 8e-h) is mostly confined to the equatorial Pacific region (Fig. 4a-d); The variability in the air temperature (Fig. 8a-d) is seen over much broader regions, reaching higher latitudes, Africa and the Middle East. Noting the above discussion of drivers vs consequences, one would expect remote surface air temperature signals, such as those seen over South Africa, North America, the Middle East etc, to likely be an effect of the LMC patterns or of the ENSO states that force the LMC variability, rather than be a driver. As mentioned above, surface air temperature over the ENSO region is likely influenced by the SST and may be expected to act as a driver of LMC variability.

For each cluster, we calculate the multiple linear regression between the temperature or precipitation and the LMC and SST,

$$AirT(t) = \alpha_T + \beta_T LMC(t) + \gamma_T SST(t) \quad (10)$$

and

$$P(t) = \alpha_P + \beta_P LMC(t) + \gamma_P SST(t), \quad (11)$$

425 respectively. The results for the coefficients β_T , γ_T , β_P and γ_P are shown in Table 1. For
 426 all cases, the linear regression captures most of the signal (R^2 under air temperature and
 427 precipitation columns mostly above 0.75). Although the LMC and SST are correlated
 428 (not independent), more of the variance of the precipitation variability is explained by
 429 the LMC variability than by the SST variability (as also seen by the fact that $\beta_P \gg \gamma_P$,
 430 remembering that all time series used are normalized). We note, though, that the LMC
 431 and the precipitation fields vary on shorter time scales than the SST, which may account
 432 for the tighter correlation. Therefore, the mechanism governing the precipitation vari-
 433 ability, while being mostly a result of the ENSO condition, is likely mediated by the LMC
 434 variability. The dependence of the air temperature on the LMC and SST is less clear,
 435 but overall it can be seen that the air temperature is better correlated with the SST. This
 436 is not surprising as one expects the 2 m air temperature to be tightly coupled with the
 437 SST, although there are areas over land where the air temperature is more free to change,
 438 not being coupled to the local SST.

439 The interaction between the LMC and temperature and precipitation fields is by
 440 no means one-way. Because the meridional circulation is driven by meridional temper-
 441 ature gradient, changes of temperature in the mid-latitudes, without any changes in the
 442 equator, will induce changes in meridional temperature gradient, which, in turn, may af-
 443 fect the meridional circulation. Similarly, if the LMC weakens, convection in the rising
 444 branch weakens, which reduces rainfall and may increase surface SW radiation, hence
 445 surface temperature. These examples further demonstrate that this is a complex and noisy
 446 system with many possible participating factors.

447 4 Summary

448 The large scale meridional circulation is a key element of the climate system, re-
 449 sponsible for the energy and moisture transport from the equatorial region to the sub-
 450 tropics. While traditionally defined as the zonally-averaged meridional circulation in the
 451 tropical region (Hadley circulation), in recent years, several studies examined the lon-
 452 gitudinal dependence of the meridional circulation via decomposition of the three-dimensional
 453 atmospheric flow into local meridional circulation (LMC), local zonal circulation, and
 454 rotational flow, using a Helmholtz decomposition into divergent and rotational flows (Keyser
 455 et al., 1989). This enables the examination of the meridional circulation at each longi-
 456 tude separately (e.g., Schwendike et al., 2014, 2015; Nguyen et al., 2018; Raiter et al.,
 457 2020). These studies provided a useful analysis of the regionality and variability of the
 458 local meridional circulation, focusing on its climatology (e.g., Raiter et al., 2020), its ENSO
 459 related variability (e.g., Schwendike et al., 2014; Nguyen et al., 2018; Staten et al., 2019),
 460 and on its response to observed climate change (e.g., Schwendike et al., 2015; Staten et
 461 al., 2019).

462 In this study we investigated the interannual variability of the LMC using hierar-
 463 chical clustering, and a Lagrangian perspective that allows the identification of the ac-
 464 tual large-scale circulation in the tropics. We use cluster analysis that allows us to iden-
 465 tify the main spatial patterns of variability of the LMC, independently of the SST vari-
 466 ability. We then examine the relation to ENSO, the MJO, and related large-scale air tem-
 467 perature and precipitation variability. We find that the interannual variability can be
 468 represented by 4 clusters, and this allows us to characterize the morphology of the LMC
 469 as expressed in its zonal and meridional shifts and expansion/contraction. Specifically,
 470 we find that most apparent is the eastward shift of the center locations during strong
 471 El Niño, and westward shift during strong La Niña-related months. We also find that
 472 during El Niño-related months, the LMC is more confined to the equatorial region, while
 473 the opposite happens during La Niña-related months, consistent with previous studies
 474 (Oort & Yienger, 1996; Caballero, 2007). These studies examined the zonal-mean Hadley
 475 circulation, and it is possible that the understanding of the local response of the LMC
 476 to ENSO-related SST will contribute to an improved understanding of the response of

477 the zonal mean as well. We supplement this morphological analysis with a calculation
 478 of Lagrangian air trajectories, showing the full changes in the interannual tropical cir-
 479 culation. We find that the east-west movement of the circulation is indeed the main vari-
 480 ability on interannual time scales, and that the LMC is dominant in setting the 3D cir-
 481 culation and its variability.

482 The cluster analysis allows us to then examine the SST patterns corresponding to
 483 each LMC variability mode as represented by the averaged SST over months belonging
 484 to each of the LMC clusters. We find that while there is no one-to-one correspondence
 485 between the the NINO3.4 or SOI ENSO indices and the LMC variability modes, the SST
 486 composites for different LMC patterns do relate to the different ENSO flavors (East and
 487 Central Pacific). The LMC is therefore affected by the variety of ENSO states (Kao &
 488 Yu, 2009; Capotondi et al., 2015). We find using regression analysis that the appropri-
 489 ate SST patterns calculated via the cluster analysis can explain a large fraction (63–71%)
 490 of the LMC temporal variance. We also find that a rather small part of the LMC vari-
 491 ance (6–8%) is explained by MJO-related variability (consistently with Schwendike et
 492 al., 2021). Further clustering-based analysis of the large-scale global response of precip-
 493 itation and surface air temperature reveals teleconnections to remote locations such as
 494 South Africa, the Middle east and North America that are likely related to the ENSO
 495 driving of the LMC.

496 To conclude, we find complex shifts and morphological changes of the longitudinally-
 497 dependent meridional circulation as part of its interannual variability, driven mostly by
 498 SST patterns. The clustering analysis which we used to examine the LMC and its re-
 499 lation to the SST allows to quantify the effect on the LMC of standard ENSO indices
 500 vs different flavors of El Niño and La Niña. The detailed dynamical/atmospheric wave
 501 mechanisms behind these findings, such as how the different drivers set the different LMC
 502 spatial patterns, are not completely clear and require further study. It seems that sim-
 503 ilar clustering analysis of projected future changes to the LMC may bring interesting in-
 504 sights.

505

506 *Acknowledgements:* This research has been supported by the Israeli Science Foun-
 507 dation (Grant 996/20), and the Weizmann Institute Helen Kimmel Center for Planetary
 508 Science. ET is supported by the NSF Climate and Large-Scale Dynamics program, grant
 509 AGS-1826635, and thanks the Weizmann Institute for its hospitality during parts of this
 510 work. Data is available via the Harvard Dataverse: <https://doi.org/10.7910/DVN/KTBSCZ>

511

Appendix A Role of the MJO in affecting LMC variability

512 To examine the possible connection of the LMC clusters to the MJO, we choose
 513 here to represent the MJO state using the daily outgoing long-wave radiation (OLR),
 514 bandpass filtered between 30–96 days, and zonal wavenumber 1–5 (Wheeler & Kiladis,
 515 1999). We take the monthly averages of the daily data and calculate the MJO-related
 516 OLR composites for each cluster (Fig. 7e-h). We again calculate the non-parametric 95%
 517 significance level for all longitudes. While the typical amplitude of the MJO composites
 518 is an order of magnitude smaller than that of the monthly climatology of the OLR field,
 519 OLR composites for clusters 2 to 4 include regions in which the composite value is sta-
 520 tistically significant, and more importantly, the structure of the signals resembles dif-
 521 ferent phases of the MJO (Wheeler & Hendon, 2004): C_2 is similar to MJO phase 6, C_3
 522 is similar to MJO phases 2 and 3, and C_4 is similar to MJO phase 5. Note that the two
 523 La Niña related clusters (C_2 and C_3) are related to opposite phases of the MJO.

524 The dependence of the LMC on the SST and MJO can be revealed by calculating
 525 the multivariate regression,

$$526 \quad LMC(t) = \alpha_L + \beta_L SST(t) + \gamma_L MJO(t). \quad (A1)$$

527 The results are shown in Table 1 (first 3 columns). Aside from C_1 , all the apparently ENSO
 528 related clusters are better explained when the MJO is included in the regression. Together,
 529 the SST and the MJO time series explain between 64% and 77% of the LMC time se-
 530 ries variance. As can be seen by the regression coefficients, the MJO contributes signif-
 531 icantly except for C_1 . When performing the regression with the MJO alone, some 6–7%
 532 of the LMC variance is explained for clusters $C_{2,3,4}$, emphasizing the role of the MJO
 533 in setting the LMC patterns. This dependency might be complicated due to the inter-
 534 play between the MJO and ENSO (e.g., Hendon et al., 2007; Tang & Yu, 2008; Liu et
 535 al., 2021). For instance, May MJO in the western Pacific leads El Niño conditions in the
 536 subsequent December (e.g., Hendon et al., 2007), while ENSO in turn impacts the MJO
 537 over the Maritime continent by shifting it south of the equator during eastern Pacific El
 538 Niño winters (Liu et al., 2021). To examine this ENSO-MJO-LMC interaction, we first
 539 remove the ENSO signal from the LMC. This is done by calculating the regression of the
 540 SST and the LMC, and then subtracting the LMC reconstructed from this regression
 541 from the full LMC time series for each cluster. This gives LMC time series that are com-
 542 pletely independent of the SST variability. This residual, explaining 32%, 42%, and 29%
 543 of the LMC variance, can be regressed with the MJO-related OLR revealing the inde-
 544 pendent effect of the MJO on the LMC. We find that for clusters C_2 , C_3 , and C_4 , the
 545 MJO explains 19%, 17%, and 21% of the residual LMC signal, respectively. Therefore,
 546 we find that the MJO is correlated with the LMC independently from the SST variabil-
 547 ity. Finally, the overall LMC relation to the MJO, while somewhat marginal, is consis-
 548 tent with the findings of several other studies (e.g., Seo et al., 2016; Schwendike et al.,
 549 2021) that analyzed the effects of different phases of the MJO on the amplitude of the
 LMC.

550 **References**

551 Ashok, K., Behera, S. K., Rao, S. A., Weng, H., & Yamagata, T. (2007). El Niño
 552 Modoki and its possible teleconnection. *J. Geophys. Res. (Oceans)*, *112*(C11),
 553 C11007. doi: 10.1029/2006JC003798

554 Caballero, R. (2007). Role of eddies in the interannual variability of Hadley cell
 555 strength. *Geophys. Res. Lett.*, *34*, 22705. doi: 10.1029/2007GL030971

556 Capotondi, A., Wittenberg, A. T., Newman, M., Di Lorenzo, E., Yu, J.-Y., Bracon-
 557 not, P., ... Yeh, S.-W. (2015). Understanding ENSO Diversity. *Bull. Am.*
 558 *Meteor. Soc.*, *96*(6), 921-938. doi: 10.1175/BAMS-D-13-00117.1

559 Chemke, R., & Polvani, L. M. (2019). Exploiting the abrupt $4 \times \text{CO}_2$ scenario to
 560 elucidate tropical expansion mechanisms. *J. Climate*, *32*(3), 859-875. doi: 10
 561 .1175/JCLI-D-18-0330.1

562 Cheng, X., & Wallace, J. M. (1993). Cluster analysis of the northern hemisphere
 563 wintertime 500-hpa height field: Spatial patterns. *J. Atmos. Sci.*, *50*(16), 2674-
 564 2696. doi: 10.1175/1520-0469(1993)050<2674:CAOTNH>2.0.CO;2

565 Dee, D., Uppala, S., Simmons, A., Berrisford, P., Poli, P., S., K., ... F., V. (2013).
 566 The ERA-Interim reanalysis: configuration and performance of the data
 567 assimilation system. *Q. J. R. Meteorol. Soc.*, *137*(656), 553-597. doi:
 568 10.1002/qj.828

569 Feldstein, S. B., & Lee, S. (2014). Intraseasonal and interdecadal jet shifts in the
 570 northern hemisphere: The role of warm pool tropical convection and sea ice. *J.*
 571 *Climate*, *27*(17), 6497-6518. doi: 10.1175/JCLI-D-14-00057.1

572 Feng, J., Chen, W., & Li, Y. (2017). Asymmetry of the winter extra-tropical tele-
 573 connections in the Northern Hemisphere associated with two types of ENSO.
 574 *Clim. Dyn.*, *48*(7-8), 2135-2151. doi: 10.1007/s00382-016-3196-2

575 Grise, K. M., Davis, S. M., Simpson, I. R., Waugh, D. W., Fu, Q., Allen, R. J., ...
 576 Staten, P. W. (2019). Recent tropical expansion: Natural variability or forced
 577 response? *J. Climate*, *32*(5), 1551-1571. doi: 10.1175/JCLI-D-18-0444.1

578 Guo, Y.-P., & Tan, Z.-M. (2018). Relationship between El Niño-Southern Oscillation
 579 and the symmetry of the Hadley circulation: role of the sea surface temperature
 580 annual cycle. *J. Climate*, *31*(13), 5319-5332. doi: 10.1175/JCLI-D-17-0788.1

581 Hartmann, D. L. (1994). *Global physical climatology*. Academic Press.

582 Hartmann, D. L. (2016). Chapter 6 - atmospheric general circulation and climate.
 583 In *Global physical climatology* (Second Edition ed., p. 159 - 193). Boston: Else-
 584 vier.

585 Held, I. M., & Soden, B. J. (2006). Robust responses of the hydrological cycle to
 586 global warming. *J. Climate*, *19*, 5686-5699. doi: 10.1175/JCLI3990.1

587 Hendon, H. H., Wheeler, M. C., & Zhang, C. (2007). Seasonal dependence of the
 588 MJO ENSO relationship. *J. Climate*, *20*(3), 531. doi: 10.1175/JCLI4003.1

589 Hersbach, H., Bell, B., Berrisford, P., Hirahara, S., Horányi, A., Muñoz-Sabater, J.,
 590 ... Thépaut, J.-N. (2020). The ERA5 global reanalysis. *Q. J. R. Meteorol.*
 591 *Soc.*, *146*(730), 1999-2049. doi: 10.1002/qj.3803

592 Horton, D. E., Johnson, N. C., Singh, D., Swain, D. L., Rajaratnam, B., & Diff-
 593 enbaugh, N. S. (2015). Contribution of changes in atmospheric circulation
 594 patterns to extreme temperature trends. *Nature*, *522*(7557), 465-469. doi:
 595 10.1038/nature14550

596 Hu, S., Cheng, J., & Chou, J. (2017). Novel three-pattern decomposition of global
 597 atmospheric circulation: Generalization of traditional two-dimensional decom-
 598 position. *Clim. Dyn.*, *49*(9-10), 3573-3586. doi: 10.1007/s00382-017-3530-3

599 Kanamitsu, M., Ebisuzaki, W., Woollen, J., Yang, S.-K., Hnilo, J. J., Fiorino, M.,
 600 & Potter, G. L. (2002). NCEP-DOE AMIP-II Reanalysis (R-2). *Bull. Am.*
 601 *Meteor. Soc.*, *83*(11), 1631-1643. doi: 10.1175/BAMS-83-11-1631

602 Kao, H.-Y., & Yu, J.-Y. (2009). Contrasting Eastern-Pacific and Central-Pacific
 603 Types of ENSO. *J. Climate*, *22*(3), 615. doi: 10.1175/2008JCLI2309.1

604 Karnauskas, K. B., & Ummenhofer, C. C. (2014, May 01). On the dynamics of the
 605 Hadley circulation and subtropical drying. *Clim. Dyn.*, *42*(9), 2259–2269. doi:
 606 10.1007/s00382-014-2129-1

607 Keyser, D., Schmidt, B. D., & Duffy, D. G. (1989). A technique for representing
 608 three-dimensional vertical circulations in baroclinic disturbances. *Mon. Weath.
 609 Rev.*, *117*(11), 2463–2494. doi: 10.1175/1520-0493(1989)117<2463:ATFRTD>2.0
 610 .CO;2

611 Liu, H., Feng, X., Tao, A., & Zhang, W. (2021). Intraseasonal Variability of Sea
 612 Level in the Western North Pacific. *J. Geophys. Res. (Oceans)*, *126*(6), e17237.
 613 doi: 10.1029/2021JC017237

614 Madden, R., & Julian, P. (1971). Detection of a 40-50 day oscillation in the zonal
 615 wind in the tropical Pacific. *J. Atmos. Sci.*, *28*(5), 702-708. doi: 10.1175/1520
 616 -0469(1971)028<0702:DOAD0I>2.0.CO;2

617 Madonna, E., Li, C., Grams, C., & Woollings, T. (2017). The link between eddy-
 618 driven jet variability and weather regimes in the north Atlantic-European
 619 sector. *Q. J. R. Meteorol. Soc.*, *143*(708), 2960-2972. doi: 10.1002/qj.3155

620 Nguyen, H., Hendon, H. H., Lim, E. P., Boschat, G., Maloney, E., & Timbal, B.
 621 (2018). Variability of the extent of the Hadley circulation in the south-
 622 ern hemisphere: a regional perspective. *Clim. Dyn.*, *50*(1), 129-142. doi:
 623 10.1007/s00382-017-3592-2

624 Oort, A. H., & Yienger, J. J. (1996). Observed interannual variability in the Hadley
 625 circulation and its connection to ENSO. *J. Climate*, *9*(11), 2751-2767. doi: 10
 626 .1175/1520-0442(1996)009<2751:OIVITH>2.0.CO;2

627 Raiter, D., Galanti, E., & Kaspi, Y. (2020). The tropical atmospheric conveyor belt:
 628 A coupled Eulerian-Lagrangian analysis of the large-scale tropical circulation.
 629 *Geophys. Res. Lett.*, *47*(10), e86437. doi: 10.1029/2019GL086437

630 Rasmusson, E. M., & Carpenter, T. H. (1982). Variations in Tropical Sea Sur-
 631 face Temperature and Surface Wind Fields Associated with the South-
 632 ern Oscillation/El Niño. *Mon. Weath. Rev.*, *110*(5), 354. doi: 10.1175/
 633 1520-0493(1982)110<0354:VITSST>2.0.CO;2

634 Saha, S., Moorthi, S., Pan, H.-L., Wu, X., Wang, J., Nadiga, S., ... Goldberg, M.
 635 (2010). The NCEP Climate Forecast System Reanalysis. *Bull. Am. Meteor.
 636 Soc.*, *91*(8), 1015-1057. doi: 10.1175/2010BAMS3001.1

637 Schwendike, J., Berry, G. J., Fodor, K., & Reeder, M. J. (2021). On the rela-
 638 tionship between the Madden-Julian Oscillation and the Hadley and Walker
 639 circulations. *J. Geophys. Res. (Atmosphere)*, *126*(4), e2019JD032117. doi:
 640 <https://doi.org/10.1029/2019JD032117>

641 Schwendike, J., Berry, G. J., Reeder, M. J., Jakob, C., Govekar, P., & Wardle, R.
 642 (2015). Trends in the local Hadley and local Walker circulations. *J. Geophys.
 643 Res. (Atmosphere)*, *120*(15), 7599-7618. doi: 10.1002/2014JD022652

644 Schwendike, J., Govekar, P., Reeder, M. J., Wardle, R., Berry, G. J., & Jakob, C.
 645 (2014). Local partitioning of the overturning circulation in the tropics and the
 646 connection to the Hadley and Walker circulations. *J. Geophys. Res. (Atmo-
 647 sphere)*, *119*(3), 1322-1339. doi: 10.1002/2013JD020742

648 Seo, K., Lee, H., & Frierson, D. (2016). Unraveling the teleconnection mechanisms
 649 that induce wintertime temperature anomalies over the northern hemisphere
 650 continents in response to the MJO. *J. Atmos. Sci.*, *73*(9), 3557-3571. doi:
 651 10.1175/JAS-D-16-0036.1

652 Simpson, I. R. (2018). Natural variability in the width of the tropics. *US CLIVAR
 653 Variations*, *16*(2), 14-20. doi: 10.5065/D69Z93QF

654 Staten, P. W., Grise, K. M., Davis, S. M., Karnauskas, K., & Davis, N. (2019).
 655 Regional widening of tropical overturning: Forced change, natural variability,
 656 and recent trends. *J. Geophys. Res. (Atmosphere)*, *124*(12), 6104-6119. doi:
 657 10.1029/2018JD030100

658 Staten, P. W., Grise, K. M., Davis, S. M., Karnauskas, K. B., Waugh, D. W., May-

659 cock, A. C., ... Son, S.-W. (2020). Tropical widening: From global variations to regional impacts. *Bull. Am. Meteor. Soc.*, 101(6), E897-E904. doi: 10.1175/BAMS-D-19-0047.1

660

661

662 Tanaka, H. L., Ishizaki, N., & Kitoh, A. (2004). Trend and interannual variability of Walker, monsoon and Hadley circulations defined by velocity potential in the upper troposphere. *Tellus A: Dynamic Meteorology and Oceanography*, 56(3), 250-269. doi: 10.3402/tellusa.v56i3.14410

663

664

665

666 Tang, Y., & Yu, B. (2008). An analysis of nonlinear relationship between the MJO and ENSO. *Journal of the Meteorological Society of Japan*, 86(6), 867-881. doi: 10.2151/jmsj.86.867

667

668

669 Totz, S., Tziperman, E., Coumou, D., Pfeiffer, K., & Cohen, J. (2017). Winter precipitation forecast in the european and mediterranean regions using cluster analysis. *Geophys. Res. Lett.*, 44(24), 12,418-12,426. doi: 10.1002/2017GL075674

670

671

672

673 Trenberth, K. E., & Stepaniak, D. (2003). Seamless poleward atmospheric energy transports and implications for the Hadley circulation. *J. Climate*, 16(22), 3706-3722. doi: 10.1175/1520-0442(2003)016<3706:SPAETA>2.0.CO;2

674

675

676 Trenberth, K. E., Stepaniak, D. P., & Caron, J. M. (2000). The global monsoon as seen through the divergent atmospheric circulation. *J. Climate*, 13(22), 3969-3993. doi: 10.1175/1520-0442(2000)013<3969:TGMAST>2.0.CO;2

677

678

679 Wang, C., Deser, C., Yu, J.-Y., DiNezio, P., & Clement, A. (2017). El niño and southern oscillation (enso): A review. In P. W. Glynn, D. P. Manzello, & I. C. Enochs (Eds.), *Coral reefs of the eastern tropical pacific: Persistence and loss in a dynamic environment* (pp. 85-106). Springer Netherlands. doi: 10.1007/978-94-017-7499-4{_}4

680

681

682

683

684 Wheeler, M., & Hendon, H. (2004). An all-season real-time multivariate MJO index: Development of an index for monitoring and prediction. *Mon. Weath. Rev.*, 132(8), 1917-1932. doi: 10.1175/1520-0493(2004)132<1917:AARMMI>2.0.CO;2

685

686

687

688 Wheeler, M., & Kiladis, G. N. (1999). Convectively Coupled Equatorial Waves: Analysis of Clouds and Temperature in the Wavenumber-Frequency Domain. *J. Atmos. Sci.*, 56(3), 374-399. doi: 10.1175/1520-0469(1999)056<0374:CCEWAO>2.0.CO;2

689

690

691

692 Wilks, D. (2011). *Statistical methods in the atmospheric sciences*. Walthan, USA: Academic Press.

693

694 Zhang, C. (2005). Madden-Julian Oscillation. *Rev. Geophys.*, 43(2). doi: 10.1029/2004RG000158

695

696 Zhang, G., & Wang, Z. (2013). Interannual variability of the Atlantic Hadley circulation in boreal summer and its impacts on tropical cyclone activity. *J. Climate*, 26(21), 8529-8544. doi: 10.1175/JCLI-D-12-00802.1

697

698